Understanding the graphene-polymer interfacial mechanical behavior via coarse-grained modeling

Wang, Yang; Nie, Wenjian; Wang, Liang; Zhang, Dawei; Niu, Kangmin; Xia, Wenjie

Published in:
Computational Materials Science

DOI:
10.1016/j.commatsci.2023.112109

Publication date:
2023

Computational Materials Science 222 (2023) 112109

Contents lists available at ScienceDirect

Computational Materials Science

journal homepage: www.elsevier.com/locate/commatsci

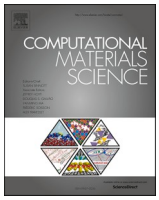

Full Length Article

Understanding the graphene-polymer interfacial mechanical behavior via coarse-grained modeling

Yang Wang [a,b], Wenjian Nie [c], Liang Wang [d], Dawei Zhang [c,*], Kangmin Niu [a,*], Wenjie Xia [c,e,f,*]

[a] School of Materials Science and Engineering, University of Science & Technology Beijing, Beijing 100083, China
[b] Zernike Institute for Advanced Materials, University of Groningen, 9747 AG Groningen, The Netherlands
[c] Department of Civil, Construction and Environmental Engineering, North Dakota State University, Fargo, ND 58108, United States
[d] Department of Engineering Mechanics, School of Naval Architecture, Ocean and Civil Engineering, Shanghai Jiao Tong University, Shanghai 200240, China
[e] Materials and Nanotechnology, North Dakota State University, Fargo, ND 58108, United States
[f] Department of Aerospace Engineering, Iowa State University, Ames, IA 50011, United States

ARTICLE INFO

Keywords:
Graphene-polymer composites
Coarse-grained modeling
Interfacial behavior
Mechanical properties
Molecular dynamics simulation

ABSTRACT

Understanding the interfacial behavior of graphene-polymer nanocomposite is a long-standing endeavor to gain deep insight into the mechanical properties of engineered structural materials. In this study, we implement the 'hard' cutoff scheme to develop a 4-1 mapping coarse-grained graphene (CGGr) model and the corresponding CG potential TersoffCG(4-1), which faithfully reproduces the honeycomb structure (bond length and angle) and mechanical properties of the graphene sheet compared to experimental results. Taking the poly(methyl methacrylate) (PMMA) and graphene sheet as a representative composite system, we establish a predictive CG modeling framework to study the interfacial behavior at a molecular level. By performing the rate-dependent interfacial separation simulations, our results reveal that lower separation velocity and thicker flexible layer can facilitate the craze fibrils formation and further enhance the toughness of the composite, which attribute to the adequate response of polymer to the graphene under lower velocity and more polymers that potentially to form fibrils under thicker flexible layer. Our work demonstrates the efficacy of TersoffCG(4-1) potential in understanding the interfacial mechanical behavior of graphene-polymer nanocomposite, offering an effective modeling strategy for performance improvement by designing the interfaces.

1. Introduction

In light of its outstanding mechanical, thermal, and electrical properties, graphene has been envisaged to be the ideal reinforcement for polymer nanocomposites (PNCs) and further implemented in diverse applications, for example, electronic and optoelectronic devices [1], field effect transistors [2], osmotic membranes [3], and portable electronics [4,5]. The origin of the outstanding performance of graphene reinforced PNCs lies in the atomic structure of graphene as a single-atomic-layer material with a honeycomb arrangement of sp^2 carbons, which grants it intrinsic strength of 130 GPa and Young's modulus of 1 TPa [6,7], and an ultra-high theoretical surface area of 2,630 m^2/g [8,9]. However, due to the strong π-π interaction (5.9 kJ/mol) between adjacent sheets, the graphene sheets are easily stacked or agglomerated in the polymeric solution during the fabrication, yielding insufficient contact between graphene and polymer matrix and further diminishing the performance of graphene reinforced PNCs [10,11]. Many researchers have been dedicated to optimizing the dispersion of graphene and the interfacial architecture between graphene and polymer, including mechanical dispersion methods (e.g., stirring, ball-milling, roll-milling or calendaring, and melt compounding processes) and non-mechanical dispersion methods (e.g., functionalization of graphene) [11,12]. However, there is still a lack of in-depth understanding of the interfacial behavior of graphene-polymer at a fundamental molecular level.

Molecular dynamics (MD) simulation method provides insightful information for investigating and designing the graphene-polymer interface structure. Jiao *et al.* [13] introduced different sizing agents at the interface of carbon fiber reinforced vinyl ester resin composite, achieving high interfacial shear strength of 62.25 MPa compared to the composite without a sizing agent of 24.39 MPa. Li *et al.* [14] studied the effect of defects on the interfacial mechanical properties of the

* Corresponding authors.
E-mail addresses: dawei.zhang.1@ndsu.edu (D. Zhang), niukm@ustb.edu.cn (K. Niu), wenjie.xia@ndsu.edu, wxia@iastate.edu (W. Xia).

https://doi.org/10.1016/j.commatsci.2023.112109
Received 6 December 2022; Received in revised form 31 January 2023; Accepted 27 February 2023
Available online 13 March 2023

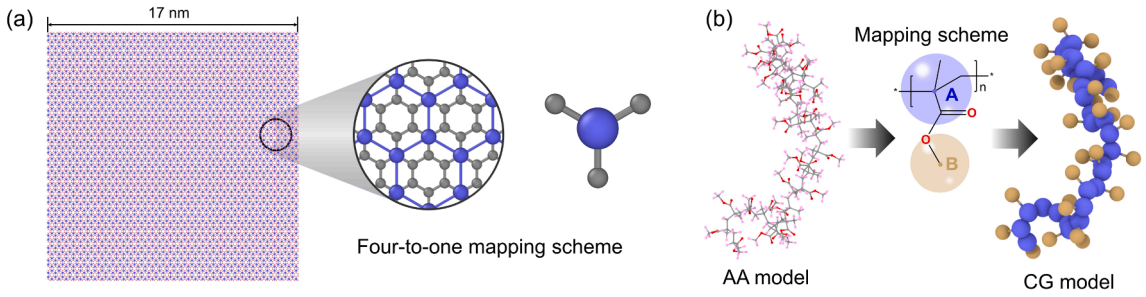

Fig. 1. (a) Schematic illustration of the four-to-one coarse-grained mapping scheme of the graphene model. The blue beads represent the coarse-grained (CG) graphene model with each bead denoting four underlying AA gray carbon atoms. (b) All-atom (AA) to coarse-grained (CG) mapping scheme for PMMA with the middle panel showing the two-bead per monomer mapping scheme. The interaction sites A and B are located at specific atoms representing the backbone group and the sidechain methyl group. (For interpretation of the references to color in this figure legend, the reader is referred to the web version of this article.)

graphene-epoxy composites by conducting normal separation and shear separation tests. It is demonstrated that the single-vacancy and double-vacancy defect graphene embedded in the epoxy would degrade the interfacial mechanical properties, but the Stone-Wales defect graphene could enhance the interfacial strength due to the enhanced π-π attractions at the graphene-epoxy interface. The effects of strain rate and defects of graphene on the separation behavior are also elaborated in other MD works [15-17]. Although those works reveal the essential information of interface properties at the atomic scale, it is still challenging to explore the interfacial mechanical performance of graphene-based PNCs approaching real devices scale due to the spatiotemporal limitation.

Coarse-grained (CG) modeling is an essential strategy for resolving the issue of limited spatiotemporal, which often eliminates less important features of a system and simultaneously retains some key structural and static properties of the atomistic model (density and radial distribution function). The energy landscape of the CG model is smoother than that of the atomistic model after coarse-graining, thus achieving the use of a larger time step for the evolution of molecular dynamics [18]. For example, Sinan *et al.* systematically developed CG models for graphene [19] and graphene oxide [20] using strain energy conservation. Whereafter, they developed several temperature-transferable CG models for the universal polymers by energy renormalization, like PMMA [21], polystyrene [22], polybutadiene [23], and polycarbonate [24], inspiring abundant subsequent research, including graphene foam [25], graphene-polymer nanocomposites [26-29], crumpled graphene sheets [30,31]. Shang *et al.* [32] developed another graphene CG model by modifying the Tersoff potential and studied the graphene assembly behavior. Although it achieves high computational efficiency because of no bonded topology in the Tersoff model, the abnormal strain hardening is a fatal problem in matching the computational mechanical properties of graphene to corresponding experimental data.

Herein, using a 'hard' cutoff scheme, we first systematically parameterize the parameters of the original Tersoff potential and develop an improved graphene CG model and corresponding TersoffCG(4-1) potential that reproduce the intrinsic mechanical properties of graphene. Taking the PMMA as a representative polymer model, we construct a PMMA-graphene nanocomposite with rather high computational efficiency of CG modeling framework, and then examine the interfacial mechanical properties. Our results show that the separation behavior of graphene from the polymer matrix is highly dependent on the pull-out velocity and the flexible layer thickness. Our findings demonstrate the reliability of the graphene CG model developed in this study, paving the way for the rational design of other graphene reinforced PNCs using mesoscale CG modeling.

2. Computational method and simulation procedures

2.1. Overview of CG models

In the present study, four carbon atoms are mapped onto one CG bead possessing a mass of 48 g/mol (Fig. 1(a)), and the graphene CG potential TersoffCG(4-1), a modified Tersoff potential, is employed to describe interactions between CG beads of graphene sheet. We denote bead C as the CG graphene bead in this work. The original environmentally dependent Tersoff potential effectively couples two body and multiple atom correlations, forming weaker inter-atomic bonds when an atom has more neighboring atoms. The original Tersoff potential function and the parameter determination are described below [33,34]:

$$E_T = \sum_i E_i = \frac{1}{2}\sum_{j\neq i} V_{ij} \tag{1}$$

$$V_{ij} = f_C(r_{ij})[f_R(r_{ij}) + b_{ij} f_A(r_{ij})] \tag{2}$$

$$f_R(r) = Ae^{-\lambda_1 r} \tag{3}$$

$$f_A(r) = -Be^{-\lambda_2 r} \tag{4}$$

$$f_C(r) = \begin{cases} 1, & r < R - D \\ \frac{1}{2}[1 - sin(\frac{\pi}{2}\cdot\frac{r-R}{D})], & R - D < r < R + D \\ 0, & r > R + D \end{cases} \tag{5}$$

$$b_{ij} = (1 + \beta^n \zeta_{ij}^n)^{-\frac{1}{2n}} \tag{6}$$

$$\zeta_{ij} = \sum_{k\neq i,j} f_C(r_{ik}) g(\theta_{ijk}) e^{[\lambda_3 (r_{ij} - r_{ik})]^m} \tag{7}$$

$$g(\theta_{ijk}) = \gamma_{ijk}(1 + \frac{c^2}{d^2} - \frac{c^2}{d^2 + (\cos\theta - \cos\theta_0)^2}) \tag{8}$$

where E_T is the total potential energy of the system, which is decomposed into a site energy E_i and a bond energy V_{ij}; $f_C(r)$ is merely a smooth cutoff function, to limit the range of the potential; and the $f_R(r)$ and $f_A(r)$ represent repulsive and attractive pair potential branches, respectively; b_{ij} is the bond order function; In addition, the indices i and j suggest different atoms of the system and r_{ij} means the distance between atom i and j. For the $f_R(r)$ and $f_A(r)$, as Eqs. (3) and (4), where A and B are the potential well depth in the energy unit and λ_1 and λ_2 control the 'width' of the potential. The exponential form of f_R and f_A is similar to the Morse potential function [35], which is based in part on analytical convenience, but also on the physical grounds that atomic orbitals decay exponentially with r [36].

Based on the mapping scheme, the initial estimation of A and B for the CG model are chosen as four times as large as that in the AA model.

Table 1
Parameters of Tersoff(AA) [34] and TersoffCG(4-1) force fields.

Parameters	Tersoff (AA)	TersoffCG(4-1)
m	3	3
γ	1	1
λ_3 (Å^{-1})	0	0
c	38,049	38,049
d	4.3484	4.3484
cos θ_0	−0.57058	−0.57058
n	0.72751	0.72751
β	0.00000015724	0.00000015724
λ_2 (Å^{-1})	2.2119	1.10595
B (eV)	346.7	1386.8
R (Å)	1.95	4.0
D (Å)	0.15	0
λ_1 (Å^{-1})	3.4879	1.74395
A (eV)	1393.6	5574.4

To keep the indexes of the expressions of repulsive and the attractive interactions consistent throughout the coarse-graining [32], parameters λ_1 and λ_2 in the graphene TersoffCG(4-1) potential are half their original values. Parameters λ_1 and λ_2 control the 'width' of the potential well, *i.e.*, the smaller λ is, the larger the well. The hexagonal structure of graphene, *i.e.*, chirality, is reserved under coarse-graining, and thus the function b_{ij} depending on the surrounding environment remains unchanged. Namely, the values of m, γ, λ_3, c, d, cosθ_0, n, and β remain the same as the counterparts in the AA model [32]. The parameters of the graphene TersoffCG(4-1) potential are summarized in Table 1, and the original Tersoff potential is also listed for comparison.

In the Tersoff potential, the parameters R and D are chosen somewhat arbitrarily, and R is chosen to include only the first-neighbor shell for most structures of interest [33,34]. In the original Tersoff potential, the energy of interaction between particles is gradually reduces to zero between R and D, which is regarded as the 'soft' cut-off scheme and caused unphysical strain hardening. Herein, to eliminate the unphysical strain hardening behavior induced by the Tersoff potential, a "hard" cut-off scheme is implemented for the CG graphene model, *i.e.*, $D = 0$, $f_C(r) = \begin{cases} 1, & r < R \\ 0, & r > R \end{cases}$, which means that a single value R is utilized for the cutoff distance [37]. We refer readers to our recent work [38] about the sixteen-to-one mapping CG graphene model, where the parameterization process is well elaborated.

For describing the interlayer interaction of CG graphene, we utilized the Lennard-Jones (L-J) 12–6 potential:

$$E_{lj} = 4\varepsilon[(\frac{\sigma}{r})^{12} - (\frac{\sigma}{r})^{6}] \tag{9}$$

where ε represents L-J potential well depth, and σ indicates the finite distance at which the inter-particle potential is zero. The equilibrium distance between two non-bonded particles is around $2^{1/6}\sigma$. The non-bonded interactions were truncated beyond 1.2 nm in this work for saving the computing resources. The L-J parameters ε and σ are extracted from the work of Ruiz et al. [19] as 0.82 kcal/mol and 3.46 Å, respectively, to describe the interactions between different graphene

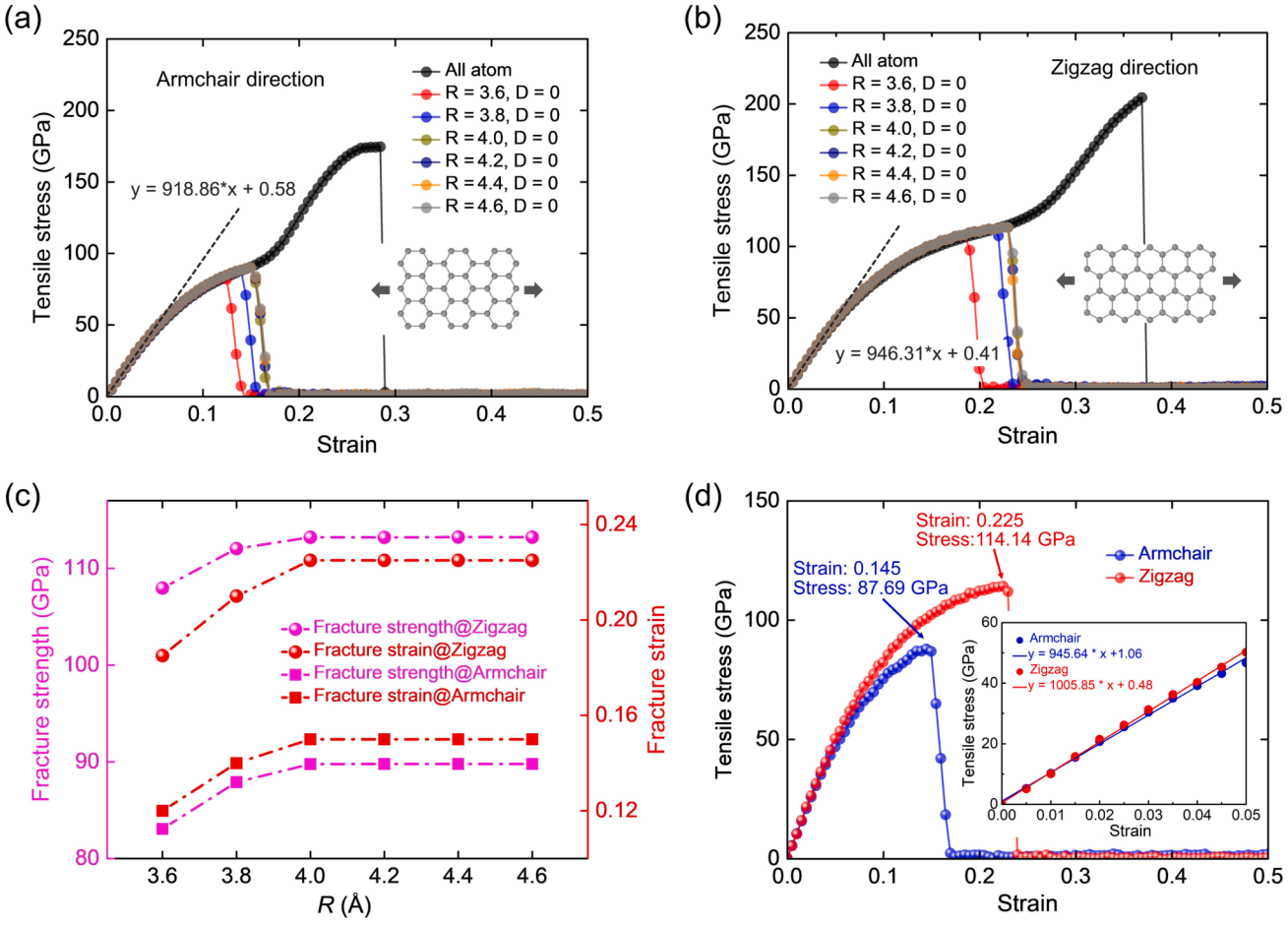

Fig. 2. Room temperature mechanical properties of AA and CG graphene models: uniaxial tensile stress–strain curves along (a) the armchair direction and (b) zigzag direction of the 4-1 mapping CG monolayer graphene model with varying cutoff distance R ranging from 3.6 to 4.6 Å, the dashed lines stand for the linear fitting of the elastic stage; (c) the calculated fracture strengths and strains of the 4-1 CG monolayer graphene with different R; and (d) engineering stress–strain curves of bilayer CG graphene model with inset showing the linear fitting of the elastic stage.

Table 2
Bonded and nonbonded potential forms and parameters of the PMMA CG model [21].

Interaction	Potential form	Parameters
AA bond	$U_{bond}(l) = k_b(l-l_0)^2$	k_b = 105.0 kcal/mol·Å^2, l_0 = 2.735 Å
AB bond	$U_{bond}(l) = k_b(l-l_0)^2$	k_b = 39.86 kcal/mol·Å^2, l_0 = 3.658 Å
AAA angle	$U_{angle}(\theta) = -k_B T \ln\left\{\sum_{i=1}^{2} a_i \cdot \exp\left[-\left(\frac{\theta-\theta_i}{b_i}\right)^2\right]\right\}$	a_1 = 2.294 × 10^{-2}, b_1 = 9.493°, θ_1 = 121.0° a_2 = 4.367 × 10^{-3}, b_2 = 6.210°, θ_2 = 158.5°
AAB angle	$U_{angle}(\theta) = \sum_{i=2}^{4} k_i \cdot (\theta-\theta_0)^i$	k_2 = 9.881 kcal/mol·rad^2, k_3 = -15.12 kcal/mol·rad^3, k_4 = 6.589 kcal/mol·rad^4, θ_0 = 1.690 rads
AAAA dihedral	$U_{dihedral}(\phi) = \sum_{i=1}^{5} a_i \cdot \cos^{i-1}(\phi)$	a_1 = 4.380 kcal/mol, a_2 = 0.8739 kcal/mol, a_3 = -0.3571 kcal/mol, a_4 = -0.2774 kcal/mol, a_5 = 0.09312 kcal/mol.
AAAB dihedral	$U_{dihedral}(\phi) = \sum_{i=1}^{5} a_i \cdot \cos^{i-1}(\phi)$	a_1 = 4.519 kcal/mol, a_2 = -0.8859 kcal/mol, a_3 = -1.692 kcal/mol, a_4 = 0.5625 kcal/mol, a_5 = 0.09562 kcal/mol.
LJ potential	$U_{lj} = 4\varepsilon[(\frac{\sigma}{r})^{12} - (\frac{\sigma}{r})^{6}]$	ε_{AA} = 0.500 kcal/mol, σ_{AA} = 5.500 Å, ε_{BB} = 1.500 kcal/mol, σ_{BB} = 4.420 Å, ε_{AB} = 0.866 kcal/mol, σ_{AB} = 4.960 Å;

flakes.

2.2. Determination of CG potential parameters

In the TersoffCG potential of graphene CG model, the parameter R is determined as 4.0 to yield the mechanical properties of the target AA graphene model. Previous studies [37,39] have revealed the successful implementation of a 'hard' cutoff scheme for two-dimensional materials, such as hexagonal BCN and graphene, achieving good agreement between predicted and measured fracture strengths. The engineering stress–strain behaviors of the armchair and zigzag AA graphene are firstly investigated with original Tersoff potential, delivering an overestimation of the fracture strength and strain when comparing experimental and simulation results. As the black lines are shown in Fig. 2(a) and (b), abnormal strain hardening appears after strain reaches 0.15 and 0.23 in the armchair and zigzag directions, respectively. Herein, by fixing $D = 0$, we systematically tune the R-value from 3.6 to 4.6 Å with an interval of 0.2 Å for the CG graphene model. It is observed that, for the armchair and zigzag deformation directions, the CG models with different R-values reproduce the stress–strain curves of the AA model before strain hardening, yielding Young's moduli (E) of 918.86 and 946.31 GPa for the armchair and zigzag directions, respectively (Fig. 2 (a) and (b)). Additionally, the fracture strength, denoted as the engineering stress of the material at the breaking point, is stabilized at 89.8 and 113.2 GPa for the CG graphene model in the armchair and zigzag conditions when $R \geq 4.0$ Å, which is consistent with the previous study of 90 and 107 GPa [6]. And the corresponding fracture strains also reach a plateau of 0.15 and 0.23 in the armchair and zigzag cases, respectively (Fig. 2(c)). Therefore, the R-value is determined as 4.0 Å. Taking interlayer interaction into consideration, the mechanical property of bilayer CG graphene is further tested in Fig. 2(d), the obtained fracture strength, fracture strain, and E are consistent with the results from the experiment and simulation [7,40,41].

The effect of R on the mechanical properties of graphene is associated with the nature of repulsive and attractive pair potentials (Fig. S2). The determination of R originated from that the energy branches f_A and f_R of the CG graphene model collapse to zero as the distance between two adjacent beads approaching the 4.0 Å. Namely, both f_A and f_R contribute small enough to the total energy of the system when R beyond 4.0 Å, corresponding to the plateau of fracture strength and strain in Fig. 2(c).

To understand the interfacial mechanics of graphene-polymer nanocomposite under room temperature (300 K), *i.e.*, pull-out test, we choose PMMA as a model polymer, which is widely utilized in combination with graphene in composite materials. As shown in Fig. 1(b), Hsu *et al.* [21] proposed a thermo-mechanically consistent CG model of PMMA, showing the density of 1.147 g/cm^3 and elastic modulus of 3.4 GPa of PMMA bulk system, which matches well with experimental results. Detailed bonded and nonbonded parameters of CG PMMA are listed in Table 2. The nonbonded interactions between different bead species of CG PMMA (bead A and B) and graphene (bead C) are determined using the Lorentz-Berthelot mixing rule, *i.e.*, the arithmetic average for $\sigma_{ab} = (\sigma_a+\sigma_b)/2$, and the geometric average for $\varepsilon_{ab} = \sqrt{\varepsilon_a{}^*\varepsilon_b}$, where a and b represent different particle type. Generally, we create the sandwich structure of interfacial model, *i.e.*, graphene-PMMA-graphene, by randomly inserting relaxed PMMA chains into the graphene slit. The detailed interfacial model construction and simulation procedures are summarized in Section S1 of Supporting Information.

2.3. Simulation details

We first build monolayer AA and CG graphene systems with a dimension of 17 × 17 nm^2, corresponding to 11,200 carbon atoms and 2800 beads per sheet, respectively (Fig. 1(a)). The original graphene Tersoff and the modified TersoffCG(4-1) potentials are utilized for the AA and CG graphene systems. Periodic boundary condition is only applied along the tensile deformation direction. The monolayer graphene was firstly minimized by using a conjugate gradient algorithm with the stop tolerance of 10^{-10} for energy and 10^{-10} Kcal/mole/Å for force, followed with 10 ps equilibration under NPT ensemble (constant number of atoms, pressure, and temperature) with a temperature of 300 K and a pressure of 1 atm. The periodic boundary condition is only applied along the tensile direction for the simulation of graphene sheet. Finally, the tensile deformation test is conducted with a relatively high strain rate of 10^9 s^{-1}, which is commonly used due to the limitation of the MD technique. A Nose-Hoover thermostat and a Nose-Hoover pressure barostat are applied to control the temperature and pressure during the simulation process. The timestep for both AA and CG monolayer graphene simulation is 1 fs. Additionally, the timestep of the CG model could be extended to 4 fs as described in the *Supporting Information* (Fig. S1). During the tensile deformation, the simulation box is corrected to ensure the monolayer graphene thickness is 3.4 Å, corresponding to the experimental and simulation results [7,42].

All modeling and simulations are implemented using LAMMPS [43], and molecular dynamics trajectories analysis is conducted with an object-oriented python toolkit, MDAnalysis (https://www.mdanalysis.org) [44]. Simulation visualizations are implemented by using the software OVITO [45].

3. Results and discussion

3.1. Mechanical properties of CG graphene model

With the developed CG potential, we firstly evaluate the structure of bilayer CG graphene by sampling the equilibration trajectory. As shown in Fig. 3, at least 500 frames are incorporated to obtain the bond and angle probability distributions of CG graphene system. It is shown that the bond length for the AA and CG models are 1.46 and 2.92 Å, respectively (Fig. 3(a)), which is consistent with our mapping scheme.

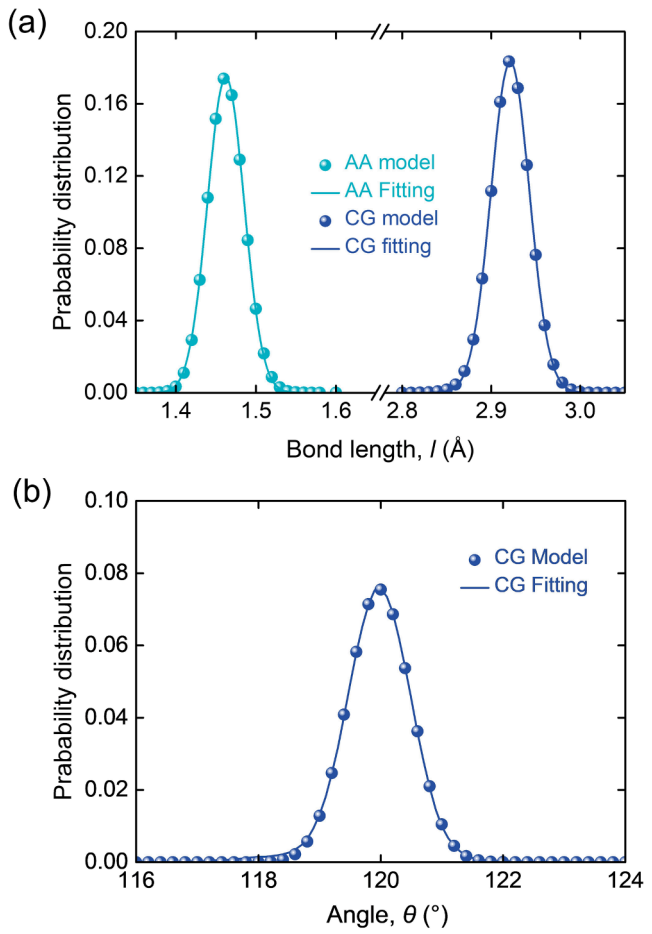

Fig. 3. Architecture structure characterization of bilayer graphene: (a) probability distributions of nearest particle distance (bond length) for the AA and CG systems with peaks located at 1.46 and 2.92 Å, respectively; (b) probability distribution of angle among three closest particles of the CG model, showing a peak located at 120°.

Noted that the Tersoff potential induces an overestimation of the bond length of graphene. From a previous study, the bond length of graphene is reported as 1.410 and 1.464 Å regarding the Airebo and Tersoff potentials, respectively [46]. The probability distribution of angle between the three nearest CG beads is a typical Gaussian function with the center of 120° (Fig. 3(b)), indicating the reasonable honeycomb structure of graphene.

Another important property is the interlayer binding energy of graphene, which plays a critical role in governing the interlayer shear behavior of the graphene assembly [47-49]. We further explore the interlayer binding energy of bilayer CG graphene, which is denoted as the negative value of the interlayer energy E_{inter}. In the present work, the interlayer energy is calculated as the van der Waals interaction (pair energy) between two adjacent graphene sheets, *i.e.*, $E_{\text{binding}} \approx -E_{\text{inter}} \approx -E_{\text{pair}}$, It is revealed that the binding energy between adjacent CG graphene layers is 218.8 ± 0.6 mJ/m^2 (Fig. S3(a)), falling in the range of 180~275 mJ/m^2 from a previous study [19]. The interlayer structure characterization shows that the interlayer distance between bilayer CG graphene is 3.41 Å (Fig. S3(b)), which is fairly consistent with previous works [7,38,42].

Nanoindentation with an Atomic Force Microscope (AFM) is a practical approach especially applicable to detecting the local mechanical properties of materials [50]. Herein, we built four graphene systems, including monolayer AA and CG graphene systems, bilayer and trilayer CG graphene systems, to systematically study the nanoindentation behavior. As shown in Fig. 4(a), four graphene systems have an identical diameter of 43 nm, and 2 nm of graphene edge is treated as the rigidly clamped boundary. Non-periodic boundary conditions are applied in three directions. The system is firstly equilibrated for 20 ps under 300 K, then a virtual rigid spherical indenter with a radius of 5 nm is placed 1 nm above the center of graphene. A constant indenter speed of 0.2 Å/ps is imposed to carry out an indentation test until the graphene is fractured. The spherical indenter exerted a force on each atom, following the relation of $F(h) = -K(d - r)^2$, where K denotes the indenter force constant and chosen as 10 eV/Å^3, d and r represent the distance from the atom to the center of the indenter and the radius of indenter, respectively.

Fig. 4(b) depicts the relationship between force and indentation depth for the four graphene systems. Because of the large ratio of indenter radius and graphene sheet radius compared to the experiment, the force and deflection behavior is described using the sphere load model [51]:

$$F = \sigma_0 \pi t \delta + \frac{Eq^3 t \cdot (r/R)^{1/4}}{R^2} \delta^3 \tag{10}$$

where F is the force collected on the indenter, δ is the central deflection or indentation depth, σ_0 is the pretension in the film, $q = 1.02$ is a dimensionless constant, $t = nh_{\text{eq}}$ is the thickness of the graphene sheet, and $h_{\text{eq}} = 0.341$ nm is the equivalent monolayer CG graphene thickness (n is the number of layers) sampled in the previous section. The sphere load model is considered due to the ratio of the radius of indenter and graphene radius is much larger than the experimental one, *i.e.*, taking r/R contribution into consideration, r and R denote the radius of indenter and graphene, respectively.

The Young's moduli (E) of the four graphene systems are determined by fitting force-indentation depth using Eq. (10). In Table 3, E of the monolayer CG graphene is fairly consistent with that AA counterpart, demonstrating the accuracy of our CG model. Within experimental error, the CG graphene systems represent a stronger elastic response as layer number increases, which can be attributed to the stronger interaction between different graphene layers as increasing layer numbers (Fig. S4). A previous study also detected a slight increase of E as the AA graphene layer increased up to six [52].

Furthermore, we study the effect of graphene radius on the mechanical properties of monolayer graphene. Taking the same nanoindentation procedure above, we choose five monolayer CG graphene models with different radii, *i.e.*, 10, 12, 14, 16, and 18 nm. It should be noted that the radius of the indenter is also changed with the graphene sheet radius to keep the r/R ratio constant compared to the multilayer graphene system. Using Eq. (10), the E of CG graphene sheets with different radii are derived and summarized in Table 4, which shows that the E is independent of graphene radius when considering r/R. However, the fracture load and indentation depth of graphene sheets with a larger radius are higher than those with a lower radius (Fig. 4(c) and Table 4).

The detailed characterization of CG graphene illustrates that our model faithfully reproduces the mechanical properties of AA counterpart and experimental results and can extend to the study of graphene assembly. We expand for readers that the 'hard' cutoff scheme could also be implemented for the AA graphene by tunning the R in the original Tersoff potential, addressing the abnormal strain hardening phenomenon. Herein, the same procedure is utilized for the AA graphene (Fig. S5), and R is determined as 2.05 Å.

3.2. Graphene-polymer interfacial behavior

Taking CG PMMA as a model polymer, we next use the CG graphene TersoffCG(4-4-1) potential to understand the interfacial mechanics of graphene-polymer nanocomposite under room temperature (300 K), *i.e.*, pull-out test. It is noted that the units of the CG graphene TersoffCG(4-1) potential parameters should be converted from *metal* to *real* to be consistent with the force field of polymer (Section S2 in Supporting Information). We construct a graphene-polymer interface model by

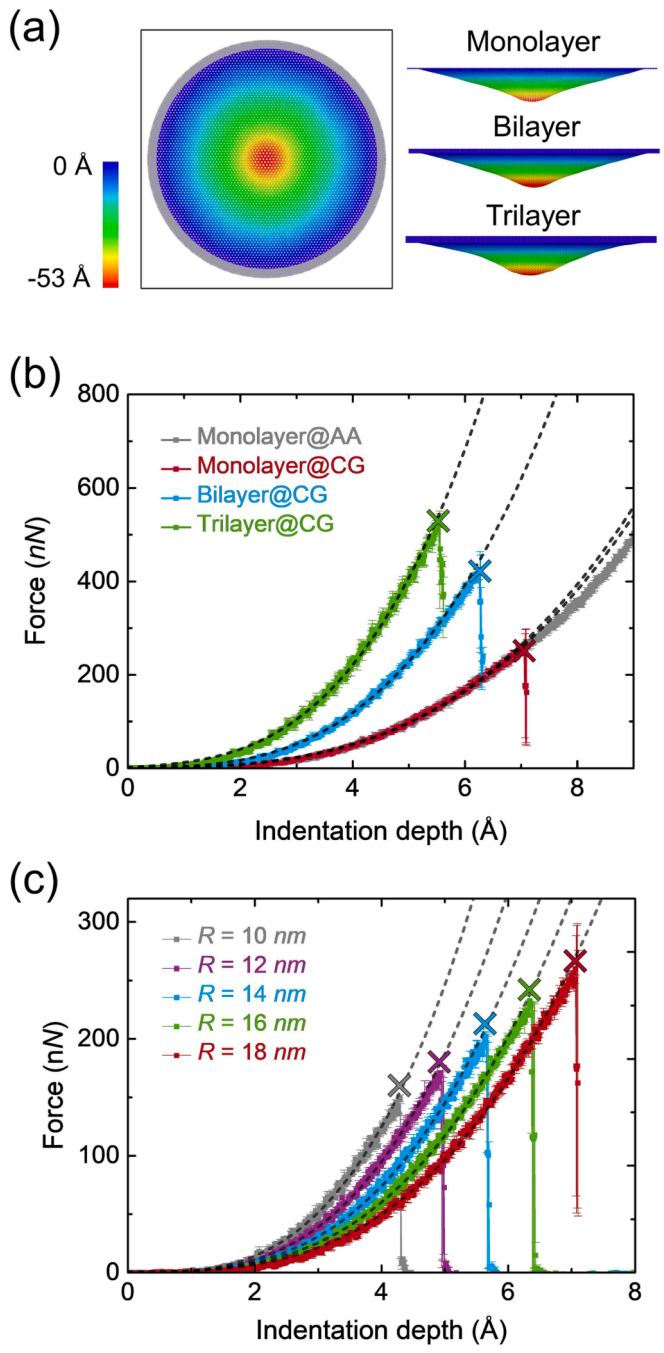

Fig. 4. (a) Height distribution for the indentation systems of monolayer, bilayer, and trilayer graphene. The gray edge indicates the clamped region and the color bar shows the height perpendicular to the graphene plane. (b) Indentation force vs. indentation depth curves for the monolayer, bilayer, and trilayer CG graphene systems, respectively. The monolayer AA graphene (gray) is also exhibited for comparison. (c) Indentation force vs. indentation depth curves for the monolayer CG graphene with varying membrane radius R. In panels (b) and (c), dashed lines represent the theoretical fitting results and the fracture loads are indicated by × symbols.

randomly inserting 200 chains with 100 monomers per chain into two rigid graphene sheets. It is noted that we choose the timestep as 4 fs in the study of the CG graphene-polymer system. The detail construction of graphene-polymer interface model is elaborated in Section S1 in Supporting Information. Fig. 5 depicts the density profile of the fully equilibrated graphene-polymer system in the vertical direction, which reveals that the polymers are tightly bound to the graphene interface

Table 3
Young's moduli of monolayer AA and CG graphene, bilayer and trilayer CG graphene systems determined from nanoindentation test.

System	E (TPa)
Monolayer@AA	1.025 ± 0.003
Monolayer@CG	1.048 ± 0.010
Bilayer@CG	1.186 ± 0.020
Trilayer@CG	1.323 ± 0.014

Table 4
Young's modulus, fracture load and depth of monolayer CG graphene systems of varying diameter determined from nanoindentation test.

Diameter (nm)	E (TPa)	Fracture load (nN)	Fracture depth (nm)
20	1.027 ± 0.005	149.4 ± 2.693	4.29
24	1.039 ± 0.004	170.9 ± 1.801	4.93
28	1.047 ± 0.004	202.1 ± 3.722	5.65
32	1.020 ± 0.016	230.0 ± 1.146	6.36
36	1.050 ± 0.010	259.6 ± 4.738	7.06

(high-density value near the interface). Additionally, the density of the interior polymer matrix is slightly higher than that of the PMMA bulk system due to this confinement model. The radius of gyration (Rg) of each PMMA chain during the equilibration process is almost keep the same (Fig. S7), indicating the fully relaxed system.

Before conducting the pull-out simulation, the condensed graphene-PMMA system is further equilibrated for 40 ps. The interfacial adhesion energy between graphene and PMMA is determined as 0.37 J/m^2 by sampling the energy between PMMA matrix and the bottom graphene sheet during equilibration, which is consistent with the reported value of 0.35 ~ 0.36 J/m^2 [53]. During the separation process, the bottom graphene sheet is treated as a rigid body due to its much higher stiffness than PMMA. Then, the bottom graphene sheet separates from the polymer matrix in the normal direction with different velocities of 0.1, 0.5, 1, 2.5, and 5 Å/ps, respectively. Fig. 6(a) shows the ultimate separation configurations of graphene-PMMA systems with increasing pull-out velocity from left to the right panel. It is revealed that under lower separation velocity, for example, 0.1, 0.5, and 1 Å/ps, PMMA chains are

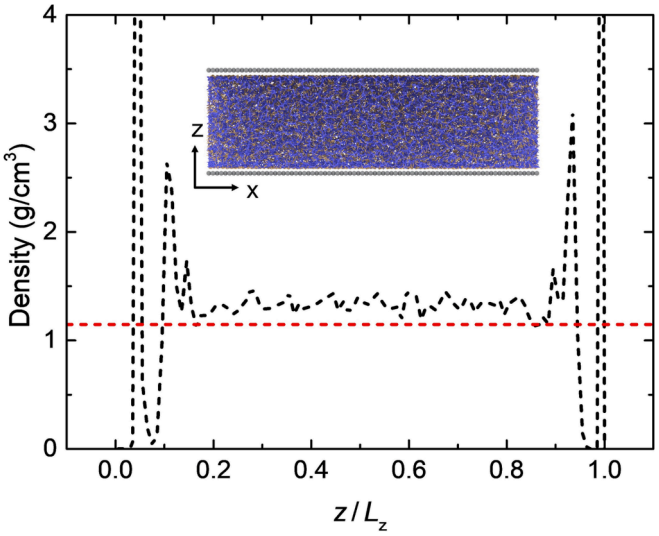

Fig. 5. Density profile of fully relaxed graphene-PMMA interface system along the vertical direction, with the inset representing the equilibrated snapshot and the red dashed line showing the bulk density of PMMA. (For interpretation of the references to color in this figure legend, the reader is referred to the web version of this article.)

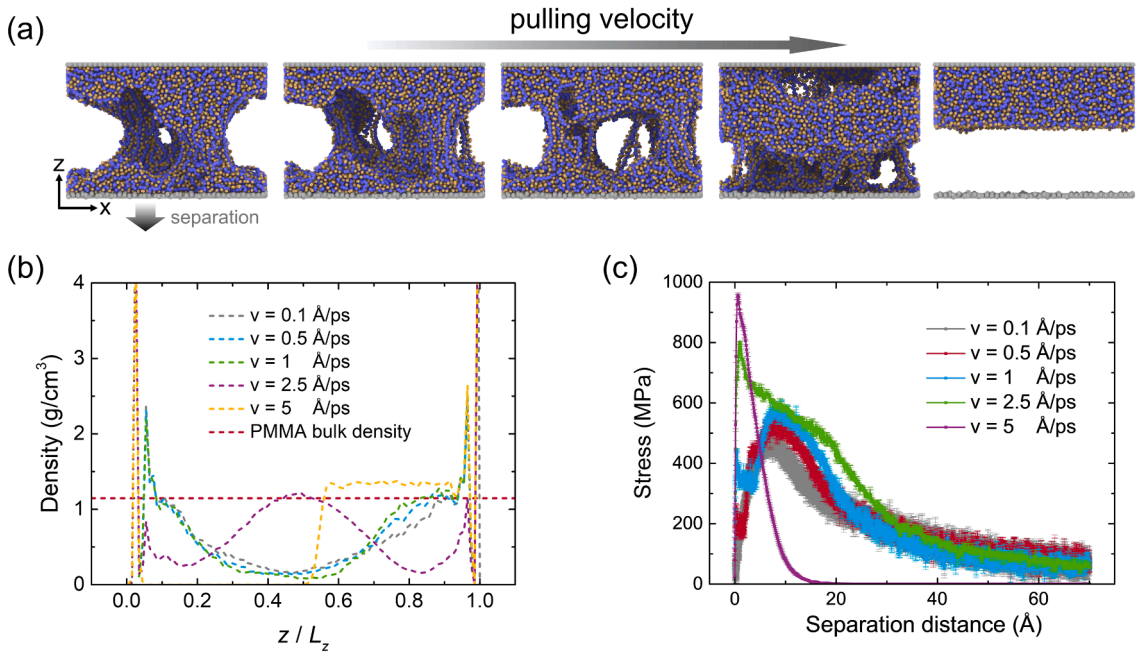

Fig. 6. (a) Schematic illustration of the ultimate pull-out configurations of graphene-PMMA systems with increasing separation velocity from the left to the right panel. (b) Density vs. z/L_z profile for the ultimate configurations of graphene-PMMA system under different separation velocities. The horizontal dashed line represents the density of the bulk PMMA system. (c) Pull-out stress vs. separation distance curves of the graphene-PMMA interface systems with varying separation velocity.

strongly attached to the bottom and top graphene sheets, forming craze fibrils and voids in the system and manifesting a similar density profile (Fig. 6(b)). Previous studies have shown that the crazing precedes during the crack propagation and greatly increases the fracture toughness [54-56]. At intermediate separation velocity, *i.e.*, 2.5 Å/ps, the adhesive force at the interface is lower than the cohesive interactions of bulk PMMA, causing the PMMA chains to separate slightly from both the top and bottom graphene layers and showing a peak density value in the middle of the system (Fig. 6(b)). Additionally, with the further expansion of the separation velocity (5 Å/ps), the fracture occurs at the interface at the initial of separation. Previous research has demonstrated as the separation velocity increases, the polymer progressively changes to complete rigidity and the polymer does not have more time to respond to deformation [17]. Fig. 6(c) reveals a typical exponential cohesive traction-separation law for separation tests under high velocity. The stress exhibits some shoulders as decreasing separation velocity, which postpones the fracture and enhances the toughness of materials due to the craze fibrils formation with different configurations.

We further explore the effect of separation velocity on the pull-out simulation by broadening separation velocity to 50 Å/ps. Fig. 7(a) indicates that the peak stress is increased as raising the separation velocity, followed by reaching a plateau value. Such phenomenon can be described using a strain-rate dependent cohesive model [57]:

$$\mathrm{T}(v) = \mathrm{T}_0 + \mathrm{T}_1 \ln(v/v_0)^2 \tag{11}$$

where v denotes the separation velocity, T_0, T_1, and v_0 are fitting constants. Herein, the maximum separation stress is considered no longer depends significantly on separation velocity when $v > 3.55$ Å/ps. To quantitatively assess the failure resistance of the graphene-PMMA interface system, we derive the fracture energy (E_f) under various separation velocity conditions and E_f is defined as [58]:

$$E_f = \int_0^{Df} \sigma(x)dx \tag{12}$$

where $\sigma(x)$ is the separation distance-dependent stress, D_f represents the

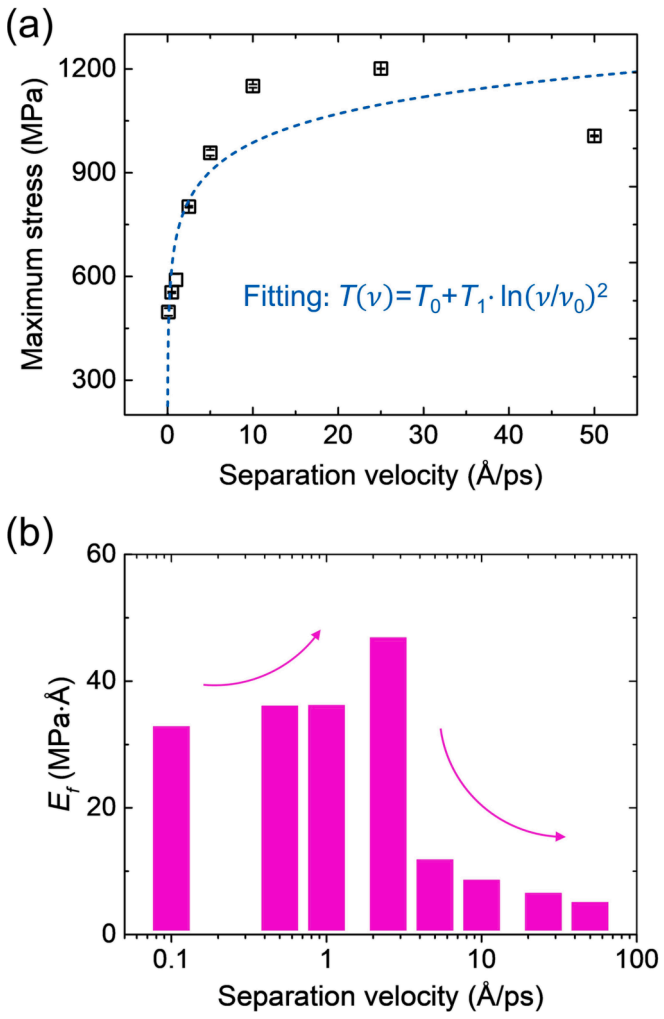

Fig. 7. (a) The maximum stress and (b) fracture energy vs. separation velocity for the graphene-PMMA systems.

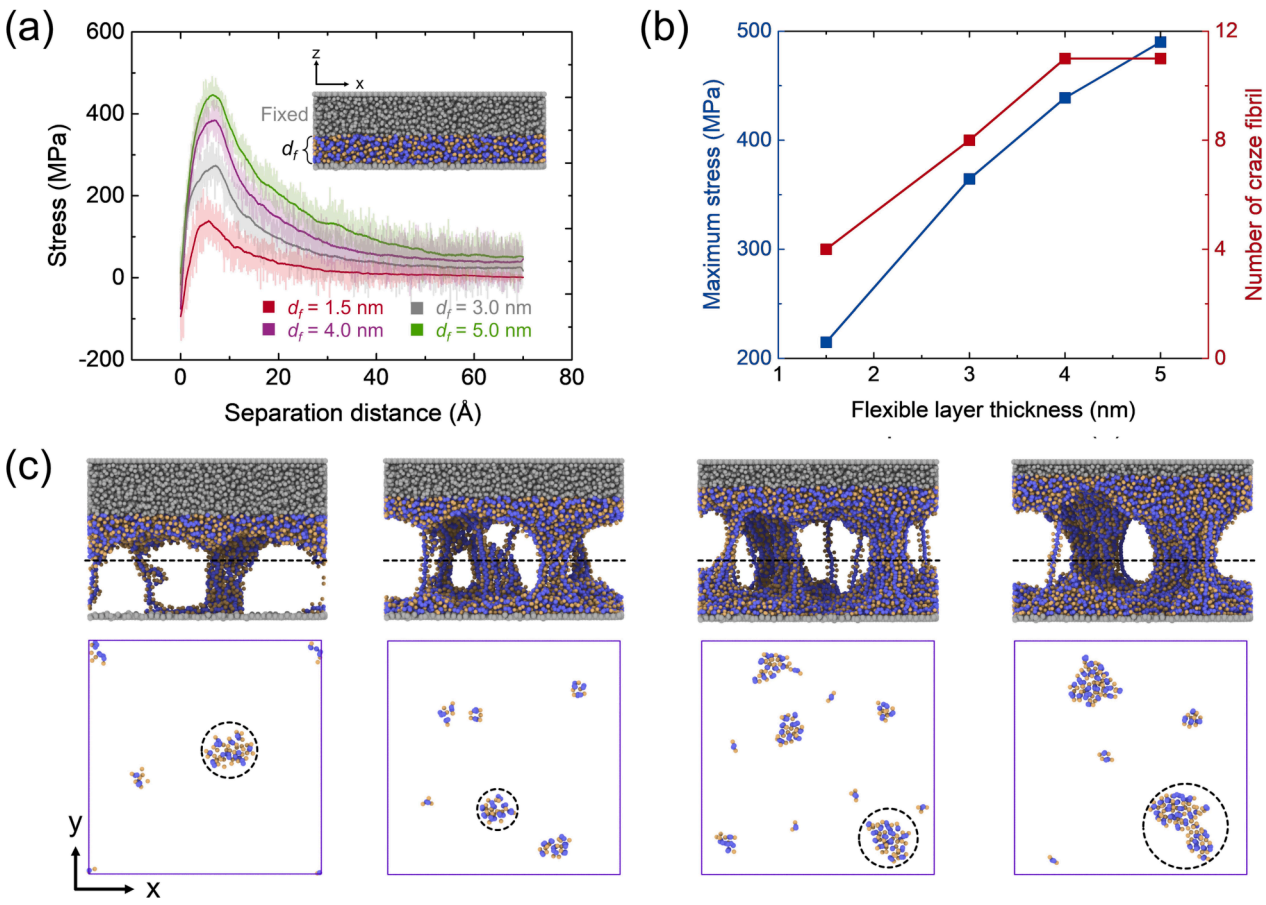

Fig. 8. (a) Pull-out stress vs. separation distance of graphene-PMMA system with different flexible layer thicknesses of d_f = 1.5, 3.0, 4.0, and 5.0 nm, respectively. The solid line represents the smoothed data and the inset refers to the schematic of the graphene-PMMA system with a flexible layer thickness of d_f. The fixed PMMA chains are in gray. (b) The peak stress, and the number of craze fibrils formed vs. flexible layer thickness of the PMMA-graphene systems. (c) Ultimate separation configurations of graphene-PMMA system with a varying flexible layer thickness of 1.5, 3.0, 4.0, and 5.0 nm from left to right, and the blue boxes below stand for the vertical view of the cross-section at the horizontal black dashed line. (For interpretation of the references to color in this figure legend, the reader is referred to the web version of this article.)

fracture distance in separating graphene-PMMA system. Herein, we set D_f equal to 70 Å for all systems since the stress decay to a small value when separation distance beyond 70 Å. Fig. 7(b) displays that the E_f increases as the increase of separation velocity from 0.1 to 2.5 Å/ps, which can be explained as the more and thicker craze fibrils formation within two graphene sheets. As separation velocity further increases, the adhesion interfacial energy between graphene and PMMA is lower than the cohesive energy of PMMA bulk system, yielding fracture at the interface of graphene and PMMA at the initial of separation. Therefore, the E_f drops significantly as shown in Fig. 7(b), revealing that the failure resistance of the system is weak.

Furthermore, we evaluate the effect of flexible PMMA layer thickness, d_f, on the separation behavior by fixing the upper polymer chain attached to the top graphene as a rigid body as the inset shown in Fig. 8 (a). The gyration radii of unperturbed PMMA model chains are about 1 nm ($R_g \approx 1$ nm) [59], so we leave a flexible PMMA layer of a certain thickness of d_f, *i.e.*, 1.5, 3.0, 4.0, and 5.0 nm, respectively. Before the pull-out simulation, the flexible layer and bottom graphene sheet are equilibrated for 40 ps under the NPT ensemble. The pull-out velocity is set to 0.1 Å/ps for all systems. Fig. 8(a) and (b) reflect that with increasing flexible layer thickness, the peak stress is enhanced during the separation process and the material toughness is improved (the area under the curve in Fig. 8(a)). Therefore, it is necessary to consider the flexible layer thickness when conducting the traction-separation test. Fig. 8(c) demonstrates the ultimate configuration of the systems. Few entire PMMA chains are allowed to deform under the condition of thinner flexible layer thickness, causing fewer craze fibrils in the system (cross section in Fig. 8(c)). As flexible layer thickness increases to greater than R_g of PMMA (gyration radius, $R_g \approx 1$ nm) [59], more entire PMMA chains contact with the bottom graphene, resulting in more craze fibrils to prevent material damage. Additionally, the craze fibrils radius tends to increase with the increase of flexible layer thickness (dashed circles in the cross-section in Fig. 8(c)). We quantify the number of craze fibrils in the cross-section area with a different flexible layer thickness in Fig. 8 (b), indicating a positive correlation. Our results show that more craze fibrils or thicker fibrils formation would potentially improve the interfacial mechanical properties and toughness of materials. Previously, we have done the in-plane tensile test using the CG modeling of PMMA/graphene layered nanocomposites [60], and we observed two different failure modes, *i.e.*, graphene yield and interfacial failure, which depends on the graphene sheet size and interfacial interactions between graphene and polymers.

4. Conclusion

In this work, we systematically develop a computationally efficient graphene CG model by modifying the original Tersoff potential using a 'hard' cutoff scheme, which eliminates the strain hardening behavior of graphene and faithfully reproduce the mechanical properties of graphene through geometric characterization, uniaxial tension and nanoindentation test. Furthermore, we extend our graphene CG model to the graphene-polymer nanocomposite and survey the separation behavior of

graphene from the PMMA matrix. It is revealed that the separation behavior is highly dependent on the pull-out velocity and flexible layer thickness. The relationship between maximum stress and separation velocity can be explained using a strain rate-dependent cohesive model. Intermediate separation velocity endows the graphene-PMMA system with maximum toughness. In general, lower velocity and thicker flexible layer could enhance the toughness of the system owing to the more and thicker craze fibrils formation.

CRediT authorship contribution statement

Yang Wang: Methodology, Software, Formal analysis, Validation, Writing – original draft, Writing – review & editing. **Wenjian Nie:** Software, Writing – review & editing. **Liang Wang:** Formal analysis, Writing – review & editing. **Dawei Zhang:** Conceptualization, Formal analysis, Writing – review & editing. **Kangmin Niu:** Supervision, Project administration, Funding acquisition, Resources, Writing – review & editing. **Wenjie Xia:** Conceptualization, Supervision, Project administration, Funding acquisition, Resources, Writing – review & editing.

Declaration of Competing Interest

The authors declare that they have no known competing financial interests or personal relationships that could have appeared to influence the work reported in this paper.

Data availability

Data will be made available on request.

Acknowledgments

The authors acknowledge the support from the U.S. National Science Foundation (NSF) under NSF CMMI Award No. 2113558. This work used supercomputing resources of the CCAST at NDSU, which were made possible in part by NSF MRI Award No. 2019077. Y.W. and K.N. acknowledge the financial support from the China Scholarship Council (CSC visiting PhD Fellowship No. 202106460027 to Y. Wang) and the University of Science & Technology Beijing. The supercomputing resources of USTB MatCom of Beijing Advanced Innovation Center for Materials Genome Engineering is also acknowledged.

Appendix A. Supplementary material

Supplementary data to this article can be found online at https://doi.org/10.1016/j.commatsci.2023.112109.

References

[1] Y. Liu, W. Hao, H. Yao, S. Li, Y. Wu, J. Zhu, et al., Solution adsorption formation of a pi-conjugated polymer/graphene composite for high-performance field-effect transistors, Adv. Mater. 30 (3) (2018) 1705377, https://doi.org/10.1002/adma.201705377.
[2] C.-J. Lin, C.-L. Liu, W.-C. Chen, Poly(3-hexylthiophene)–graphene composite-based aligned nanofibers for high-performance field effect transistors, J. Mater. Chem. C 3 (17) (2015) 4290–4296, https://doi.org/10.1039/c5tc00399g.
[3] W. Zhao, H. Liu, Y. Liu, M. Jian, L. Gao, H. Wang, et al., Thin-film nanocomposite forward-osmosis membranes on hydrophilic microfiltration support with an intermediate layer of graphene oxide and multiwall carbon nanotube, ACS Appl. Mater. Interfaces 10 (2018) 34464–34474, https://doi.org/10.1021/acsami.8b10550.
[4] C. Pavlou, M.G. Pastore Carbone, A.C. Manikas, G. Trakakis, C. Koral, G. Papari, et al., Effective EMI shielding behaviour of thin graphene/PMMA nanolaminates in the THz range, Nat. Commun. 12 (1) (2021) 4655, https://doi.org/10.1038/s41467-021-24970-4.
[5] G. Anagnostopoulos, P.N. Pappas, Z. Li, I.A. Kinloch, R.J. Young, K.S. Novoselov, et al., Mechanical stability of flexible graphene-based displays, ACS Appl. Mater. Interfaces 8 (34) (2016) 22605–22614, https://doi.org/10.1021/acsami.6b05227.
[6] H. Zhao, K. Min, N.R. Aluru, Size and chirality dependent elastic properties of graphene nanoribbons under uniaxial tension, Nano Lett. 9 (8) (2009) 3012–3015, https://doi.org/10.1021/nl901448z.
[7] C. Lee, X. Wei, J.W. Kysar, J. Hone, Measurement of the elastic properties and intrinsic strength of monolayer graphene, Science 321 (5887) (2008) 385–388, https://doi.org/10.1126/science.1157996.
[8] A. Peigney, C. Laurent, E. Flahaut, R.R. Bacsa, A. Rousset, Specific surface area of carbon nanotubes and bundles of carbon nanotubes, Carbon 39 (4) (2001) 507–514, https://doi.org/10.1016/S0008-6223(00)00155-X.
[9] M.J. McAllister, J.-L. Li, D.H. Adamson, H.C. Schniepp, A.A. Abdala, J. Liu, et al., Single sheet functionalized graphene by oxidation and thermal expansion of graphite, Chem. Mater. 19 (18) (2007) 4396–4404, https://doi.org/10.1021/cm0630800.
[10] L.-C. Tang, Y.-J. Wan, D. Yan, Y.-B. Pei, L. Zhao, Y.-B. Li, et al., The effect of graphene dispersion on the mechanical properties of graphene/epoxy composites, Carbon 60 (2013) 16–27, https://doi.org/10.1016/j.carbon.2013.03.050.
[11] L. Dong, Z. Chen, X. Zhao, J. Ma, S. Lin, M. Li, et al., A non-dispersion strategy for large-scale production of ultra-high concentration graphene slurries in water, Nat. Commun. 9 (1) (2018) 76, https://doi.org/10.1038/s41467-017-02580-3.
[12] P. Govindaraj, A. Sokolova, N. Salim, S. Juodkazis, F.K. Fuss, B. Fox, et al., Distribution states of graphene in polymer nanocomposites: a review, Compos. B Eng. 226 (2021), 109353, https://doi.org/10.1016/j.compositesb.2021.109353.
[13] W. Jiao, T. Zheng, W. Liu, W. Jiao, R. Wang, Molecular dynamics simulations of the effect of sizing agent on the interface property in carbon fiber reinforced vinyl ester resin composite, Appl. Surf. Sci. 479 (2019) 1192–1199, https://doi.org/10.1016/j.apsusc.2019.02.157.
[14] M. Li, H. Zhou, Y. Zhang, Y. Liao, H. Zhou, The effect of defects on the interfacial mechanical properties of graphene/epoxy composites, RSC Adv. 7 (73) (2017) 46101–46108, https://doi.org/10.1039/c7ra08243f.
[15] S.C. Chowdhury, J.W. Gillespie, Strain-rate dependent mode I cohesive traction laws for glass fiber-epoxy interphase using molecular dynamics simulations, Compos. B Eng. 237 (2022), 109877, https://doi.org/10.1016/j.compositesb.2022.109877.
[16] J. Di, Z. Lei, Z. Ren, R. Mao, R. Bai, T. Wang, et al., Interfacial characterization in defective graphene/PET substrate structure through traction separation models: a molecular dynamics study, Comput. Mater. Sci. 211 (2022), 111540, https://doi.org/10.1016/j.commatsci.2022.111540.
[17] J. Jose, T.B. Varkey, N. Swaminathan, Insights into traction-separation phenomena of graphene-cis-1,4-polyisoprene interface using molecular dynamics, Polymer 122 (2017) 280–295, https://doi.org/10.1016/j.polymer.2017.06.038.
[18] S. Kmiecik, D. Gront, M. Kolinski, L. Wieteska, A.E. Dawid, A. Kolinski, Coarse-grained protein models and their applications, Chem. Rev. 116 (2016) 7898–7936, https://doi.org/10.1021/acs.chemrev.6b00163.
[19] L. Ruiz, W. Xia, Z. Meng, S. Keten, A coarse-grained model for the mechanical behavior of multi-layer graphene, Carbon 82 (2015) 103–115, https://doi.org/10.1016/j.carbon.2014.10.040.
[20] Z. Meng, R.A. Soler-Crespo, W. Xia, W. Gao, L. Ruiz, H.D. Espinosa, et al., A coarse-grained model for the mechanical behavior of graphene oxide, Carbon 117 (2017) 476–487, https://doi.org/10.1016/j.carbon.2017.02.061.
[21] D.D. Hsu, W. Xia, S.G. Arturo, S. Keten, Systematic method for thermomechanically consistent coarse-graining: a universal model for methacrylate-based polymers, J. Chem. Theory Comput. 10 (6) (2014) 2514–2527, https://doi.org/10.1021/ct500080h.
[22] W. Xia, J. Song, C. Jeong, D.D. Hsu, F.R. Phelan, J.F. Douglas, et al., Energy-renormalization for achieving temperature transferable coarse-graining of polymer dynamics, Macromolecules 50 (2017) 8787–8796, https://doi.org/10.1021/acs.macromol.7b01717.
[23] J. Song, D.D. Hsu, K.R. Shull, F.R. Phelan, J.F. Douglas, W. Xia, et al., Energy renormalization method for the coarse-graining of polymer viscoelasticity, Macromolecules 51 (10) (2018) 3818–3827, https://doi.org/10.1021/acs.macromol.7b02560.
[24] W. Xia, N.K. Hansoge, W.S. Xu, F.R. Phelan Jr., S. Keten, J.F. Douglas, Energy renormalization for coarse-graining polymers having different segmental structures, Sci. Adv. (2019;5(4):eaav4683.), https://doi.org/10.1126/sciadv.aav4683.
[25] Z. Shen, H. Ye, C. Zhou, M. Kroger, Y. Li, Size of graphene sheets determines the structural and mechanical properties of 3D graphene foams, Nanotechnology 29 (10) (2018), 104001, https://doi.org/10.1088/1361-6528/aaa612.
[26] M. Zhou, J. Liu, H. Yang, L. Zhang, A multi-scale analysis on reinforcement origin of static and dynamic mechanics in graphene-elastomer nanocomposites, Compos. Sci. Technol. 228 (2022), https://doi.org/10.1016/j.compscitech.2022.109617.
[27] Y. Wang, Z. Meng, Mechanical and viscoelastic properties of wrinkled graphene reinforced polymer nanocomposites - effect of interlayer sliding within graphene sheets, Carbon 177 (2021) 128–137, https://doi.org/10.1016/j.carbon.2021.02.071.
[28] J. Yang, D. Custer, C. Chun Chiang, Z. Meng, X.H. Yao, Understanding the mechanical and viscoelastic properties of graphene reinforced polycarbonate nanocomposites using coarse-grained molecular dynamics simulations, Comput. Mater. Sci. 191 (2021), 110339, https://doi.org/10.1016/j.commatsci.2021.110339.
[29] T. Li, Z. Meng, S. Keten, Interfacial mechanics and viscoelastic properties of patchy graphene oxide reinforced nanocomposites, Carbon 158 (2020) 303–313, https://doi.org/10.1016/j.carbon.2019.10.039.
[30] A.B. Croll, Y. Liao, Z. Li, W.M.A. Jayawardana, T. Elder, W. Xia, Sticky crumpled matter, Matter 5 (6) (2022) 1792–1805, https://doi.org/10.1016/j.matt.2022.04.029.
[31] Y. Liao, Z. Li, X.W. Fatima, Size-dependent structural behaviors of crumpled graphene sheets, Carbon 174 (2021) 148–157, https://doi.org/10.1016/j.carbon.2020.12.006.

[32] J. Shang, Q. Yang, X. Liu, New coarse-grained model and its implementation in simulations of graphene assemblies, J. Chem. Theory Comput. 13 (2017) 3706–3714, https://doi.org/10.1021/acs.jctc.7b00051.
[33] J. Tersoff, Empirical interatomic potential for carbon, with applications to amorphous carbon, Phys.Rev. Lett. 61 (1988) 2879–2882, https://doi.org/10.1103/PhysRevLett.61.2879.
[34] J. Tersoff, New empirical approach for the structure and energy of covalent systems, Phys. Rev. B 37 (1988) 6991–7000, https://doi.org/10.1103/PhysRevB.37.6991.
[35] P.M. Morse, Diatomic molecules according to the wave mechanics II. Vibrational levels, Phys. Rev. B 34 (1929) 57–64, https://doi.org/10.1103/PhysRev.34.57.
[36] G.C. Abell, Empirical chemical pseudopotential theory of molecular and metallic bonding, Phys. Rev. B 31 (1985) 6184–6196, https://doi.org/10.1103/PhysRevB.31.6184.
[37] Y.-Y. Zhang, Q.-X. Pei, Z.-D. Sha, Y.-W. Zhang, A molecular dynamics study of the mechanical properties of h-BCN monolayer using a modified Tersoff interatomic potential, Phys. Lett. A 23 (2019) 2821–2827, https://doi.org/10.1016/j.physleta.2019.05.055.
[38] Y. Wang, K. Niu, Y. Wu, Multiscale modelling of graphene sheet and its application in laminated composites, Compos. Struct. 276 (2021), 114416, https://doi.org/10.1016/j.compstruct.2021.114416.
[39] G. Rajasekaran, R. Kumar, A. Parashar, Tersoff potential with improved accuracy for simulating graphene in molecular dynamics environment, Mater. Res. Express 3 (3) (2016), 035011, https://doi.org/10.1088/2053-1591/3/3/035011.
[40] F. Liu, P. Ming, J. Li, Ab initio calculation of ideal strength and phonon instability of graphene under tension, Phys. Rev. B 76 (2007), 064120, https://doi.org/10.1103/PhysRevB.76.064120.
[41] M.Z. Hossain, T. Hao, B. Silverman, Stillinger-Weber potential for elastic and fracture properties in graphene and carbon nanotubes, J. Phys.: Condens. Matter 30 (5) (2018), 055901, https://doi.org/10.1088/1361-648X/aaa3cc.
[42] Y.K. Koh, M.-H. Bae, D.G. Cahill, E. Pop, Reliably counting atomic planes of few-layer graphene (n > 4), ACS Nano 5 (2011) 269–274, https://doi.org/10.1021/nn102658a.
[43] S. Plimpton, Fast parallel algorithms for short-range molecular dynamics, J. Comp. Phys. 117 (1) (1995) 1–19, https://doi.org/10.1006/jcph.1995.1039.
[44] N. Michaud-Agrawal, E.J. Denning, T.B. Woolf, O. Beckstein, MDAnalysis: a toolkit for the analysis of molecular dynamics simulations, J. Comput. Chem. 32 (10) (2011) 2319–2327, https://doi.org/10.1002/jcc.21787.
[45] A. Stukowski, Visualization and analysis of atomistic simulation data with OVITO-the open visualization tool, Modell. Simul. Mater. Sci. Eng. 18 (2010), 015012, https://doi.org/10.1088/0965-0393/18/1/015012.
[46] F. Memarian, A. Fereidoon, G.M. Darvish, Graphene Young's modulus: Molecular mechanics and DFT treatments, Superlattices Microstruct. 85 (2015) 348–356, https://doi.org/10.1016/j.spmi.2015.06.001.
[47] H. Shin, J. Kim, H. Lee, O. Heinonen, A. Benali, Y. Kwon, Nature of interlayer binding and stacking of sp-sp^2 hybridized carbon layers: a quantum Monte Carlo study, J. Chem. Theory Comput. 13 (2017) 5639–5646, https://doi.org/10.1021/acs.jctc.7b00747.
[48] J. Berashevich, T. Chakraborty, On the nature of interlayer interactions in a system of two graphene fragments, J. Phys. Chem. C 115 (50) (2011) 24666–24673, https://doi.org/10.1021/jp2095032.
[49] W. Xia, L. Ruiz, N.M. Pugno, S. Keten, Critical length scales and strain localization govern the mechanical performance of multi-layer graphene assemblies, Nanoscale 8 (12) (2016) 6456–6462, https://doi.org/10.1039/c5nr08488a.
[50] D.E. Martínez-Tong, A.S. Najar, M. Soccio, A. Nogales, N. Bitinis, M.A. López-Manchado, et al., Quantitative mapping of mechanical properties in polylactic acid/natural rubber/organoclay bionanocomposites as revealed by nanoindentation with atomic force microscopy, Compos. Sci. Technol. 104 (2014) 34–39, https://doi.org/10.1016/j.compscitech.2014.08.030.
[51] X. Tan, J. Wu, K. Zhang, X. Peng, L. Sun, J. Zhong, Nanoindentation models and Young's modulus of monolayer graphene: a molecular dynamics study, Appl. Phys. Lett. 102 (2013), 071908, https://doi.org/10.1063/1.4793191.
[52] T. Zhong, J. Li, K. Zhang, A molecular dynamics study of Young's modulus of multilayer graphene, J. Appl. Phys. 125 (2) (2019), 175110, https://doi.org/10.1063/1.5091753.
[53] G. Wang, E. Gao, Z. Dai, L. Liu, Z. Xu, Z. Zhang, Degradation and recovery of graphene/polymer interfaces under cyclic mechanical loading, Compos. Sci. Technol. 149 (2017) 220–227, https://doi.org/10.1016/j.compscitech.2017.06.004.
[54] J. Wang, P.J. in 't Veld, M.O. Robbins, T. Ge, Effects of coarse-graining on molecular simulation of craze formation in polymer glass, Macromolecules 55 (4) (2022) 1267–1278, https://doi.org/10.1021/acs.macromol.1c01969.
[55] J. Wang, T. Ge, Crazing reveals an entanglement network in glassy ring polymers, Macromolecules 54 (16) (2021) 7500–7511, https://doi.org/10.1021/acs.macromol.1c01080.
[56] J.G. Ethier, L.F. Drummy, R.A. Vaia, L.M. Hall, Uniaxial deformation and crazing in glassy polymer-grafted nanoparticle ultrathin films, ACS Nano 13 (11) (2019) 12816–12829, https://doi.org/10.1021/acsnano.9b05001.
[57] C.S. Meyer, B.Z. Haque, J.W. Gillespie Jr, Bridging length scales from micro to mesoscale through rate-dependent traction-separation law predictions, Compos. B Eng. 231 (2022), 109558, https://doi.org/10.1016/j.compositesb.2021.109558.
[58] D. Hu, X. Gu, F. Yang, Z. Zhou, W. Bo, B. Cui, et al., Atomic mechanisms of separation failure at the asphalt–aggregate interface and its dependence on aging and rejuvenation: insights from molecular dynamics simulations and DFT calculations, Appl. Surf. Sci. 598 (2022), 153775, https://doi.org/10.1016/j.apsusc.2022.153775.
[59] A.F. Behbahani, S.M. Vaez Allaei, G.H. Motlagh, H. Eslami, V.A. Harmandaris, Structure, dynamics, and apparent glass transition of stereoregular poly(methyl methacrylate)/graphene interfaces through atomistic simulations, Macromolecules 51 (19) (2018) 7518–7532, https://doi.org/10.1021/acs.macromol.8b01160.
[60] W. Xia, J. Song, Z. Meng, C. Shao, S. Keten, Designing multi-layer graphene-based assemblies for enhanced toughness in nacre-inspired nanocomposites, Mol. Syst. Des. Eng. 1 (1) (2016) 40–47, https://doi.org/10.1039/c6me00022c.